bioRxiv preprint doi: https://doi.org/10.1101/2021.04.17.440277; this version posted April 19, 2021. The copyright holder for this preprint (which was not certified by peer review) is the author/funder. All rights reserved. No reuse allowed without permission.

Visualization of subcortical structures in non-human primates in vivo by Quantitative Susceptibility Mapping at 3T MRI

Abbreviated title:

Macaque subcortical visualization by QSM at 3T MRI

Authors and Affiliations:

Atsushi Yoshida[1], Frank Q Ye[2], David K Yu[2], David A Leopold[2,3], Okihide Hikosaka[1]

[1] Laboratory of Sensorimotor Research, National Eye Institute, National Institutes of Health, Bethesda, MD 20892.

[2] Neurophysiology Imaging Facility, National Institute of Mental Health, National Institute for Neurological Disorders and Stroke, National Eye Institute, National Institutes of Health, Bethesda, MD 20892.

[3] Laboratory of Neuropsychology, National Institute of Mental Health, National Institutes of Health, Bethesda, MD 20892.

Keywords: Non-human primate, Macaque monkey, MRI, QSM, Magnetic susceptibility

Correspondence to:

Atsushi Yoshida, MD, PhD

Laboratory of Sensorimotor Research, National Eye Institute, National Institutes of Health, Bethesda, MD 20892.

Email: yoshidaatsushi0113@gmail.com

bioRxiv preprint doi: https://doi.org/10.1101/2021.04.17.440277; this version posted April 19, 2021. The copyright holder for this preprint (which was not certified by peer review) is the author/funder. All rights reserved. No reuse allowed without permission.

Author contribution: A.Y., F.Y., D.Y., D.L., and O.H. designed research; A.Y., F.Y., and D.Y. performed research; A.Y. analyzed data; A.Y. wrote the paper; and A.Y., F.Y., D.Y., D.L., and O.H. edited the paper.

Conflict of interest: All authors claim that there are no conflicts of interest.

Acknowledgments: This research was supported by the Intramural Research Program at the National Institutes of Health, National Eye Institute, and JSPS KAKENHI Grant (Grant-in-Aid for Fostering Joint International Research (A), 17KK0180). MRI scanning was carried out in the Neurophysiology Imaging Facility Core (National Institute of Mental Health, National Institute of Neurological Disorders and Stroke, and National Eye Institute). We thank D. Parker, A. Lopez, D. O'Brien, V.L. McLean, I. Bunea, G. Tansey, M.K. Smith, A.M. Nichols, D. Yochelson, J.W. McClurkin, A.V. Hays, and J. Fuller-Deets for technical assistance.

bioRxiv preprint doi: https://doi.org/10.1101/2021.04.17.440277; this version posted April 19, 2021. The copyright holder for this preprint (which was not certified by peer review) is the author/funder. All rights reserved. No reuse allowed without permission.

Highlights

- NHP subcortical structures are challenging to see in conventional T1w and T2w images
- We applied quantitative susceptibility mapping (QSM) to identify them easily
- QSM clearly visualized basal ganglia and cerebellar nucleus of high brain iron content
- CNRs of some subcortical nucleus were significantly higher in QSM
- QSM values of several subcortical nucleus increased with age

Abbreviation

AC	anterior commissure
CNR	contrast-to-noise ratio
CdB	body of caudate nucleus
CdH	head of caudate nucleus
CdT	tail of caudate nucleus
DBS	deep brain stimulation
DN	dentate nucleus
GPe	globus pallidus external segment
GPi	globus pallidus internal segment
IC	internal capsule
GRE	gradient echo
MCP	middle cerebellar peduncle
MPRAGE	magnetization prepared rapid gradient echo
MRI	magnetic resonance imaging
NHP	non-human primate

bioRxiv preprint doi: https://doi.org/10.1101/2021.04.17.440277; this version posted April 19, 2021. The copyright holder for this preprint (which was not certified by peer review) is the author/funder. All rights reserved. No reuse allowed without permission.

70	NMT	NIMH macaque template
71	OT	optic tract
72	Put	putamen
73	QSM	quantitative susceptibility mapping
74	ROI	region of interest
75	SARM	subcortical atlas of the rhesus macaque
76	SN	substantia nigra
77	SPACE	sampling perfection with application optimized contrasts using different flip angle
78	evolution	
79	STN	subthalamic nucleus
80	T1w	T1-weighted
81	T2w	T2-weighted
82	TE	echo time
83	TR	repetition time
84	3D	three-dimensional
85	VP	ventral pallidum
86		
87		
88		
89		
90		
91		
92		

bioRxiv preprint doi: https://doi.org/10.1101/2021.04.17.440277; this version posted April 19, 2021. The copyright holder for this preprint (which was not certified by peer review) is the author/funder. All rights reserved. No reuse allowed without permission.

Abstract

Magnetic resonance imaging (MRI) is now an essential tool in the field of neuroscience involving non-human primates (NHP). Structural MRI scanning using T1-weighted (T1w) or T2-weighted (T2w) images provides anatomical information, particularly for experiments involving deep structures such as the basal ganglia and cerebellum. However, for certain subcortical structures, T1w and T2w images fail to reveal important anatomical details. To better visualize such structures in the macaque brain, we applied a relatively new method called quantitative susceptibility mapping (QSM), which enhances tissue contrast based on the local tissue magnetic susceptibility. To evaluate the visualization of important structures, we quantified the the contrast-to-noise ratios (CNRs) of the ventral pallidum (VP), globus pallidus external and internal segments (GPe and GPi), substantia nigra (SN), subthalamic nucleus (STN) in the basal ganglia and the dentate nucleus (DN) in the cerebellum. For these structures, the QSM method significantly increased the CNR, and thus the visibility, beyond that in either the T1w or T2w images. In addition, QSM values of some structures were correlated to the age of the macaque subjects. These results indicate that the QSM method can enable the clear identification of certain subcortical structures that are invisible in more traditional scanning sequences.

bioRxiv preprint doi: https://doi.org/10.1101/2021.04.17.440277; this version posted April 19, 2021. The copyright holder for this preprint (which was not certified by peer review) is the author/funder. All rights reserved. No reuse allowed without permission.

1. Introduction

Magnetic resonance imaging (MRI) plays an essential role in neuroscience research involving non-human primates (NHP). For example, structural MRI scanning to obtain T1-weighted (T1w) or T2-weighted (T2w) images provides important details of brain structure that guides the penetration of microelectrodes for recording neural activity or cannulae for injecting any of a range of agents into the brain, including recent virally expressed proteins for optogenetic and chemogenetic perturbation of brain circuits (Amita et al., 2020; Bonaventura et al., 2019; El-Shamayleh & Horwitz, 2019; Eldridge et al., 2016; Maeda et al., 2020; Nagai et al., 2016;). Prior to the advent of MRI, NHP neurophysiologists relied on postmortem histological evaluation of brain sections under the microscope to determine definitively the area in which they had targeted with their recordings or injections. The capacity to check recording location using MRI has thus greatly increased the accuracy and efficiency of electrophysiology experiments in non-human primates.

Increasingly, modern viral methods utilize anatomical MRI data to identify targets for stereotaxic injection (Fredericks et al., 2020). While some targets are readily visible using standard MRI contrast, others are not. For example, it has been virtually impossible to use T1w or T2w contrasts to detect boundaries within subcortical nuclei of the basal ganglia (e.g., the globus pallidus, the substantia nigra) and the cerebellum (e.g., the dentate nucleus). This is because the signal intensities of these gray matter structures are, in fact, similar to those of the white matter around them. As a result, many functionally distinct substructures whose differential targeting may be of potential interest remain undifferentiated even in high quality MRI atlases of the macaque brain (Seidlitz et al., 2018).

bioRxiv preprint doi: https://doi.org/10.1101/2021.04.17.440277; this version posted April 19, 2021. The copyright holder for this preprint (which was not certified by peer review) is the author/funder. All rights reserved. No reuse allowed without permission.

Quantitative susceptibility mapping (QSM) is a relatively new MRI acquisition approach for enhancing tissue contrast (Liu et al., 2011; Wu et al., 2012; Li et al., 2011). This method exploits subtle differences in local tissue magnetic susceptibility, allowing for the visibility of otherwise hidden gray matter substructures, particularly those rich in iron. Quantitative susceptibility values across the brain are reconstructed from the MRI phase images acquired using a 3D gradient echo (GRE) sequence. Previous human studies have shown that the QSM method offers substantial visualization of internal tissue contrast for structures such as the basal ganglia, whose components vary in their level of iron deposition. For example, within the basal ganglia, this method allows for the visualization and segmentation of gray matter structures with similar T1w and T2w contrasts, such as the globus pallidus external segment (GPe), globus pallidus internal segment (GPi), subthalamic nucleus (STN), substantia nigra (SN) (Liu et al., 2013b). As a result, the QSM method has been clinically used to guide neurosurgical implantation of electrodes in the STN, a primary target in deep brain stimulation (DBS) for Parkinson's patients (de Hollander et al., 2014; Dimov et al., 2018). While the QSM should be similarly useful to neuroscientists focusing on these and other subcortical structures in monkeys, to our knowledge this method has not been previously used in NHPs at 3T.

The present study applies the QSM acquisition protocol to the macaque brain *in vivo* to examine its feasibility and robustness in this species. The results demonstrate clear contrast images of deep gray matter structure, including the visualization of subnuclei of the basal ganglia and the cerebellum that is unclear in T1w and T2w images.

2. Materials and methods

Subjects

bioRxiv preprint doi: https://doi.org/10.1101/2021.04.17.440277; this version posted April 19, 2021. The copyright holder for this preprint (which was not certified by peer review) is the author/funder. All rights reserved. No reuse allowed without permission.

Six adult male rhesus monkeys (Macaca mulatta), three younger monkeys (M1 (8 years and three months old, 10kg), M2 (8 years and five months old, 13kg), and M3 (8 years and five months old, 11kg)), and three older monkeys (M4 (13 years and four months old, 12kg), M5 (14 years and six months old, 14kg), and M6 (14 years and seven months old, 14kg)), participated in this study. Head post implant were present in three of the six subjects to immobilize the head. All experimental procedures followed National Institutes of Health guidelines and were approved by the Animal Care and Use Committee of the National Eye Institute.

Animal preparation for MRI

All MR images were acquired under anesthesia to avoid image artefact by head motion. Monkey's head was fixed in an MRI-compatible stereotaxic frame. For anesthesia, atropine (0.05 mg/kg, i.m.) was initially injected and ketamine (10 mg/kg, i.m.) and dexmedetomidine (0.01 mg/kg, i.m.) were used for induction. Additional ketamine (5 mg/kg, i.m.) and dexmedetomidine (0.01 mg/kg, i.m.) were injected for maintenance.

Imaging Protocols and QSM reconstruction

MR imaging of all six monkeys was performed in a clinical 3T MR imaging system (MAGNETOM Prisma; Siemens Healthcare, Erlangen, Germany) using a human 15-channel human knee coil. T1w images were acquired using MPRAGE whose parameters were as follows: 0.5 mm isotropic, FOV 128 x 128 x 112 mm, matrix 256 x 256 slices per slab 224, sagittal orientation, number of averages 4, TR 2200 ms, TE 2.23 ms, TI 900 ms, flip angle 8. T2w images were acquired using SPACE (Mugler et al., 2000) with the following parameters: 0.5 mm isotropic, FOV 128 x 128 x 112 mm, matrix 256 x 256, slice per slab 224, TR 3200 ms, TE 562

bioRxiv preprint doi: https://doi.org/10.1101/2021.04.17.440277; this version posted April 19, 2021. The copyright holder for this preprint (which was not certified by peer review) is the author/funder. All rights reserved. No reuse allowed without permission.

ms, number of averages 2. QSM was obtained with a 3D multi-echo gradient-echo (GRE) sequence with TR 50 ms, TE: 3.65/10.11/16.73/23.35/29.97/36.59/43.21 ms, bandwidth 280 Hz/pixel, flip angle 15, FOV 128 x 128 x 57.6 mm, matrix 320 x 320 x 144, number of averages 1.

QSM images were reconstructed from the phase images from 3D GRE with multiple echo, as described previously in detail (Liu et al., 2015; Wang et al., 2015) and summarized in Fig. 1A. This reconstruction process consisted of three main steps: (1) *Unwrapping of the phase images*. This step was necessary because any angle of proton phase shift lying outside the range between $-\pi$ and π is folded back in the image, and this folding was abundant in raw phase images with longer TE. (2) *High-pass filtering of phase image*. This step compensated for the dominating susceptibility influence of the tissue-air interface ('background phase') and focused instead on local tissue phase images. (3) *Dipole deconvolution*. This step was performed to map the magnetic susceptibility in each voxel. Many algorithms to solve this dipole inversion problem have been developed (Li et al., 2011; Liu et al., 2009; Liu et al., 2012; Tang et al., 2013; Wharton et al., 2010). In this study, we used the Morphology Enabled Dipole Inversion (MEDI) method (Bollmann et al., 2019; Liu et al., 2011; Liu et al., 2012; Liu et al., 2013a; Liu et al., 2018). These three steps were performed by using the MEDI toolbox on MATLAB2019 (Liu et al., 2012, http://pre.weill.cornell.edu/mri/pages/qsm.html).

Quantitative image evaluation

To evaluate the visibility of the ventral pallidum (VP), globus pallidus external segment (GPe), globus pallidus internal segment (GPi), substantia nigra (SN), subthalamic nucleus (STN) in the basal ganglia, and the dentate nucleus (DN) in the cerebellum in T1w, T2w, and QSM, the

bioRxiv preprint doi: https://doi.org/10.1101/2021.04.17.440277; this version posted April 19, 2021. The copyright holder for this preprint (which was not certified by peer review) is the author/funder. All rights reserved. No reuse allowed without permission.

contrast-to-noise ratios (CNRs) were calculated by the following formula: $CNR = |I_{ROI} - I_{wm}|/\sigma_{wm}$, where I_{ROI} is the average signal intensity of the region of interest (ROI) and I_{wm} is the average signal intensity of white matter near ROI (Dimov et al., 2018). σ_{wm} represents the noise measurement calculated as the standard deviation of I_{wm}. First of all, to create ROIs semi-automatically, each subject's T1w image was aligned to the standard NIMH macaque template (NMT v2.0) using analysis pipeline (*NMT_subject_align*) with software AFNI (Cox 1996; Jung et al., 2021; Seidlitz et al., 2018) (Fig. 1B (a), (b)). Secondly, the subcortical atlas of the rhesus macaque (SARM) for NMT (Hartig et al., 2021) was inversely transformed to the subject T1w image (Fig. 1B (c), (d)) by AFNI's *3dNwarpApply* with output files from NMT_subject_align pipeline (inverse of linear transformation matrix and non-linear warp field). Finally, if the modification of ROIs was needed, we edited it manually, referring to the QSM, T1w, and T2w images. Afterward, these masks were applied to the T2w and QSM images for calculating the CNRs after resampled the voxel size of the QSM from 0.4 mm to 0.5 mm as well as the T1w and T2w. We used the left hemisphere for determining ROIs. For measuring the CNR of ROIs, we defined as I_{wm} the ipsilateral anterior commissure (AC) (for the VP in Fig. 2), the internal capsule (IC) (for the GPe and GPi in Fig. 3), the optic tract (for the SN and STN in Fig. 4), the part of the ipsilateral middle cerebellar peduncle (for the DN in Fig. 5).

Statistical analysis

Kruskal-Wallis tests were performed to compare the differences in the CNRs among T1w, T2w, and QSM and in the subcortical structures (VP, GPe, GPi, SN, STN, and DN) followed by the post hoc multiple comparisons (Dunn-Sidak test) were executed. To investigate whether the QSM values in each subcortical structure were correlated with monkeys' age, we also assessed

bioRxiv preprint doi: https://doi.org/10.1101/2021.04.17.440277; this version posted April 19, 2021. The copyright holder for this preprint (which was not certified by peer review) is the author/funder. All rights reserved. No reuse allowed without permission.

Spearman's rank correlation test between monkeys' age and the mean QSM values in each ROIs. For multiple comparisons, we applied the Benjamini-Hochberg procedure controlling at a significance level of $\alpha = 0.05$ (Benjamini et al, 1995). These statistical analyses were performed using MATLAB Statistics and Machine Learning Toolbox.

3. Results

Visualization of subcortical structures

Figs. 2, 3, 4, and 5 show comparisons of subcortical structures among T1w, T2w, and QSM for several subcortical regions of the brain marked by low contrast in conventional anatomical MRI scans. The upper panel in each figure shows MR images from one of the younger monkeys (monkey M1, 8 y/o), while the lower panel illustrates images from one of the older monkeys (monkey M6, 14 y/o). In each case, QSM highlighted certain substructures as having higher susceptibility, reflecting a higher level of iron content than neighboring areas. For example, QSM applied to the pallidal structure (Fig. 2C) shows distinct boundaries among the VP, GPe, and AC, in contrast to the conventional images where the boundaries were indistinct because the structures have similar T1w and T2w values. Fig. 3 illustrates the value of QSM in identifying the boundary of another portion of the globus pallidus, namely the medial medullary lamina between the GPe and GPi (indicated by yellow-colored arrowhead in Fig.3C and F), also subtle or absent in T1w and T2w scans. In Figure 4, the QSM further highlights the substantial nigra (SN) of the midbrain, and the nearby GPe components of the globus pallidus. Although the SN was detectable in QSM from both younger and older monkeys, the subthalamic nucleus (STN) was subtle even in QSM from the older monkey (Fig.4F). QSM also illustrated the position and detailed shape of the dentate nucleus in the cerebellum (Fig. 5), which was nearly invisible in

bioRxiv preprint doi: https://doi.org/10.1101/2021.04.17.440277; this version posted April 19, 2021. The copyright holder for this preprint (which was not certified by peer review) is the author/funder. All rights reserved. No reuse allowed without permission.

T1w and T2w images. This marked difference probably stems from the elevated iron deposition in the dentate nucleus compared to other cerebellar nuclei, such as the nucleus interpositus and nucleus medialis, whose hyperintensity is observed to be less.

Quantitative Results

To quantitatively evaluate visualization of subcortical structures in QSM, T1w, and T2w, we measured the CNRs of them in each MR image and performed statistical tests. Figure 6 presents the results of comparing the CNRs. The Kruskal-Wallis test and post hoc test revealed that the CNRs of all 6 subcortical structures in QSM were significantly higher than those in T1w and/or T2w ($P < 0.05$, Dunn-Sidak). We also assessed the regression analysis (Pearson's rank correlation test) to investigate whether the mean QSM value of each ROI correlated with subjects' ages (Fig. 7). The QSM values of the VP, GPe, GPi were significantly correlated with ages corrected by Benjamini-Hochberg procedure.

4. Discussion

Our results indicate that quantitative susceptibility mapping in the macaque offers a marked improvement in the visualization of certain subcortical structures, significantly heightening the CNRs over T1w and/or T2w images. Most notably, QSM enabled a clear and efficient differentiation of the pallidum (VP, GPe, and GPi), substantia nigra, and cerebellar nucleus (DN) from the white matter around them. Thus, this anatomical scanning approach may be advantageous for neuroscientists targeting these and nearby structures for the recording of neuronal activity or the injection of viral vectors or other agents. To our knowledge, this is the first study for the feasibility of QSM in the macaque brain in vivo at 3T MRI, with only one previous article applying QSM to the macaque brain at 9.4T (Wen et al., 2019).

bioRxiv preprint doi: https://doi.org/10.1101/2021.04.17.440277; this version posted April 19, 2021. The copyright holder for this preprint (which was not certified by peer review) is the author/funder. All rights reserved. No reuse allowed without permission.

QSM is based on the local measurement of magnetic susceptibility tissue, which strongly reflects the concentration of paramagnetic unpaired electrons. This sensitivity makes QSM able to identify and delineate the boundaries of the structures prone to iron deposition as ferritin, such as the nuclei in the basal ganglia (the VP, GPe, GPi, and SN) and the cerebellum (DN) (Schweser et al., 2011; Schafer et al., 2012). Iron deposition in these structures occurs from a young age in humans (Bilgic et al., 2012; Keuken et al., 2017; Li et al., 2014; Persson et al., 2015) and probably also in macaque monkeys. Actually, the CNRs of QSM, even in younger monkeys around 8 years old, were higher, and the QSM values in subcortical structures were positively correlated with ages.

The improved CNRs of the subcortical structures compared to T1w and T2w, QSM allows macaque researchers to investigate the substructure of deep subcortical regions in a way that has not previously been possible using anatomical MRI methods. This method may be particularly useful for neuroscientists in NHP who investigate the functions of the basal ganglia and the cerebellum. Clear visualization of the structures in QSM can increase the efficiency of researchers by decreasing the number of electrode or needle penetrations required for neuronal recording the injection of chemical substances such as pharmacological agents or viral vectors for genetical manipulations. Several human neurosurgery researchers have recently reported that QSM is useful for surgeries to put electrodes for deep brain stimulation (DBS) for Parkinson's disease or dystonia patients. Similar to the work shown here, these studies showed that QSM at 3T MRI (Dimov et al., 2018; Li et al., 2020; Wei et al., 2019) and 7T MRI (de Hollander et al., 2014) visualized targets of the DBS (the STN, GPi, and centromedian thalamic nucleus). For macaque research, this method, combined with T1w images for the grid in the neuronal recording chamber, will allow us to achieve more precise targeting in focusing on the subcortical

bioRxiv preprint doi: https://doi.org/10.1101/2021.04.17.440277; this version posted April 19, 2021. The copyright holder for this preprint (which was not certified by peer review) is the author/funder. All rights reserved. No reuse allowed without permission.

299 regions. The adoption of QSM may also help avoid the need to euthanize monkeys merely to
300 check the position of electrodes or injections in histological sections.

301 One possible application of this method is the incorporation of QSM contrast into new
302 macaque MRI brain atlases, such as the National Institute of Mental Health Macaque Template
303 (NMT), which is a high-quality contrast made from T1w images of 31 macaque monkeys (Jung
304 B et al., 2021; Seidlitz et al., 2018). Whereas the NMT shows clear structures in the basal
305 ganglia, the T1w images, particularly in younger monkeys, do not provide sufficient contrast to
306 segment the substantia nigra (SN). This is why one can't get precise alignment between the
307 standard template and the native structure image. In fact, the results of aligning the SN region in
308 the SARM atlas to the native subject's T1w images were not accurate (all SN ROIs were out of
309 alignment in the superior direction (Fig. S1)), and thus we needed to manually modify ROIs for
310 the SN of all subjects. To use QSM image for registration to NMT and SARM will provide
311 precisely the SN discrimination, and it help us to enable the more accurate analysis, in which, for
312 example, it is allowed for analysis of functional MRI (fMRI) data (task fMRI or resting-state
313 fMRI) to use more accurate seed or ROI. QSM in this study also clearly illustrated the DN in the
314 cerebellum. The DN receives projections mainly from Crus I and Crus II in the cerebellar
315 hemisphere, which are assumed to be involved in the cognitive functions (Bostan et al, 2018; Ito
316 2008; Middleton et al., 2001; Strick et al., 2009). Many researchers in NHP have been interested
317 in investigating the cognitive functions of the DN (Ashmore et al., 2013; Kunimatsu et al., 2018;
318 Lu et al., 1998; Ohmae et al., 2013). Thus, QSM may be useful not only for neuronal recording
319 from the DN but also for more precision seed analysis of the DN in the fMRI research in NHP.

320 Finally, there are a few limitations of this method that should be stated explicitly. First,
321 QSM is highly sensitive to tissue with substances that induce susceptibility change. After

bioRxiv preprint doi: https://doi.org/10.1101/2021.04.17.440277; this version posted April 19, 2021. The copyright holder for this preprint (which was not certified by peer review) is the author/funder. All rights reserved. No reuse allowed without permission.

322 penetration of electrode or needle, hemosiderin deposit will happen naturally in the affected
323 brain tissue. Because hemosiderin includes iron, QSM illustrates hemosiderin deposit as
324 hyperintensity. Thus, it may not be easy to see the accurate borders of the subcortical structures
325 in QSM after several electrode or needle penetrations. Therefore, it may be better to carry out
326 QSM scanning before any penetrations or early in the experiment. Second, iron deposition in the
327 subcortical structures starts during adolescence in humans. Thus, the QSM method does not
328 show hyperintensity in these structures in childhood and may therefore not be useful to guide
329 experiments in infant monkeys (Bilgic et al., 2012; Li et al., 2014; Persson et al., 2015).
330 In summary, our results suggest that QSM visualized the subcortical structures more clearly than
331 the conventional T1w and T2w. It may be useful for a range of neuroscience applications in NHP
332 that benefit from the clear visualization of structural divisions among subcortical regions.
333
334 ***Data Availability***
335 MR images data related to this publication will be available upon reasonable request from the
336 corresponding author (A.Y.).
337
338
339
340
341
342
343
344

bioRxiv preprint doi: https://doi.org/10.1101/2021.04.17.440277; this version posted April 19, 2021. The copyright holder for this preprint (which was not certified by peer review) is the author/funder. All rights reserved. No reuse allowed without permission.

345 ***Figures***

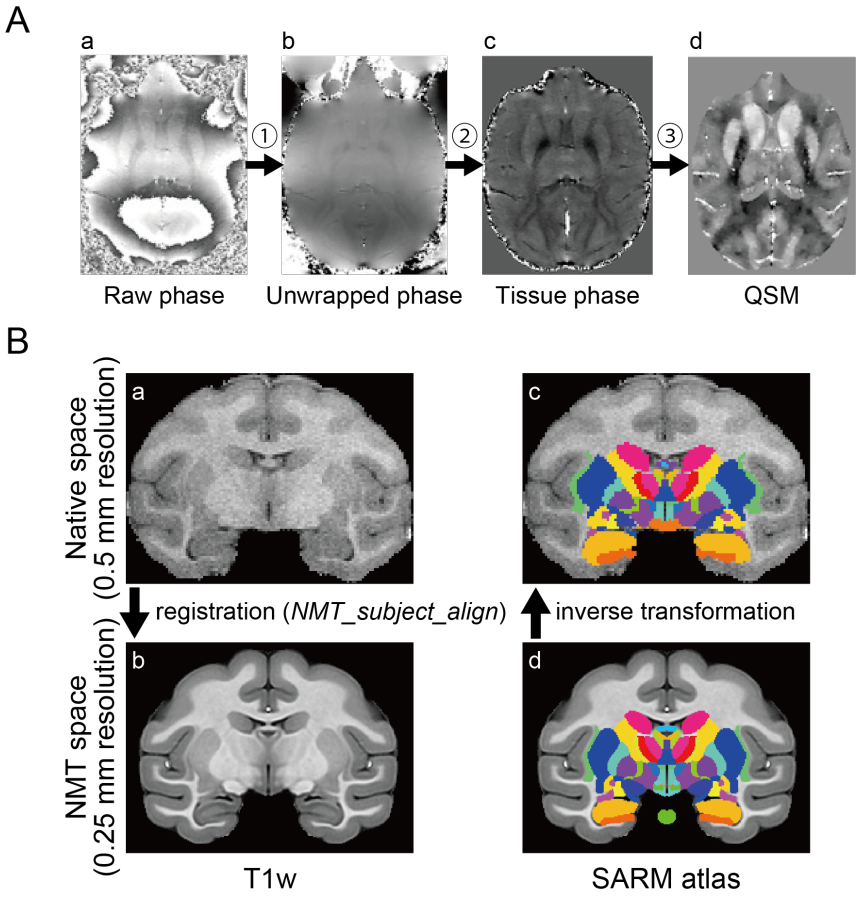

346

347 **Figure 1.** Imaging preprocesses. (A) Overview of QSM processing. QSM is reconstructed from
348 3D gradient echo phase images with different TE. There are three main steps in the processing
349 from the raw phase image to QSM; ① unwrapping ② background phase removal by high-pass
350 filtering, ③ inverse problem solution by performing a dipole deconvolution. (B) Automatic ROI
351 creation using SARM atlas. SARM atlas in NMT space was inversely transformed into each
352 subject's space (from (d) to (c)) using output from alignment of a subject's T1w image to NMT
353 (from (a) to (b)).

354

355

356

bioRxiv preprint doi: https://doi.org/10.1101/2021.04.17.440277; this version posted April 19, 2021. The copyright holder for this preprint (which was not certified by peer review) is the author/funder. All rights reserved. No reuse allowed without permission.

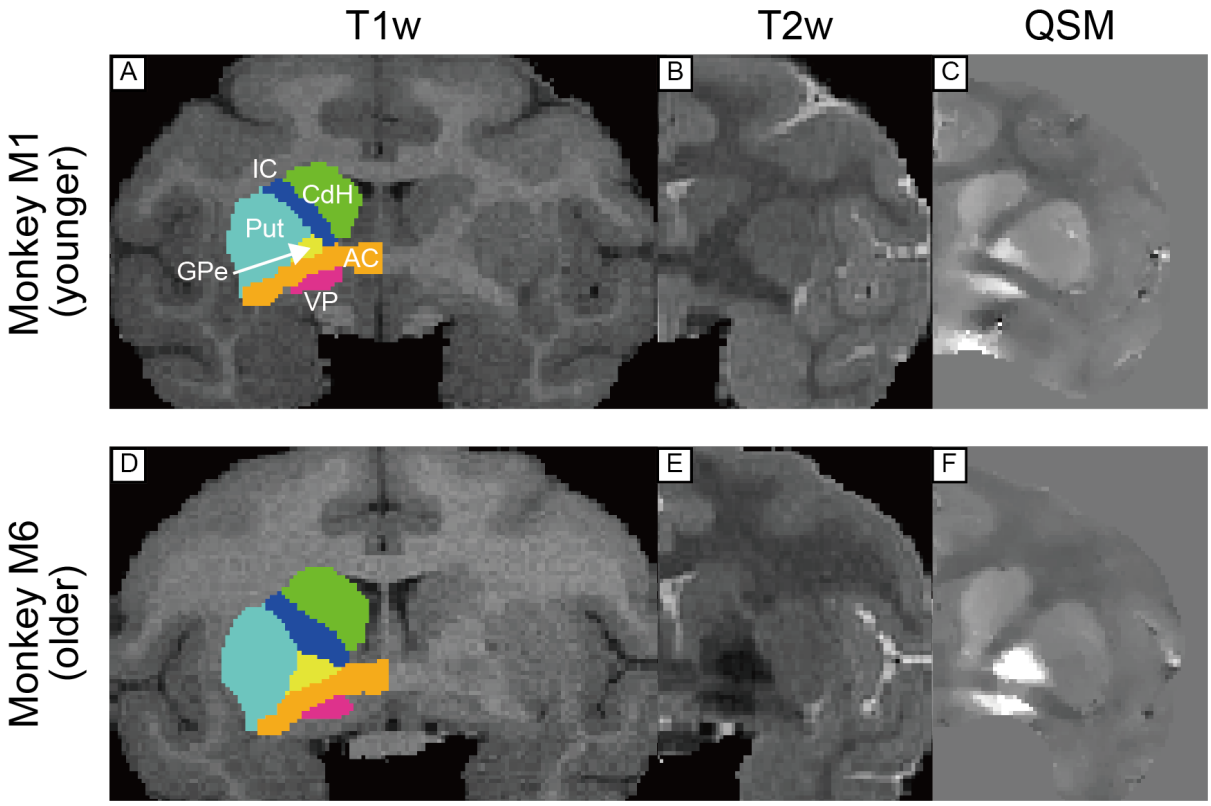

Figure 2. T1w, T2w, and QSM coronal images including anterior commissure (AC) in a younger ((A), (B), and (C)) and older monkeys ((D), (E), and (F)). Colored drawings in left hemisphere in T1w images indicate ROIs created from SARM atlas. These were used for calculations of CNR and mean QSM values. Abbreviations: AC, anterior commissure. CdH, head of caudate nucleus. GPe, globus pallidus external segment. IC, internal capsule. Put, putamen. VP, ventral pallidum.

bioRxiv preprint doi: https://doi.org/10.1101/2021.04.17.440277; this version posted April 19, 2021. The copyright holder for this preprint (which was not certified by peer review) is the author/funder. All rights reserved. No reuse allowed without permission.

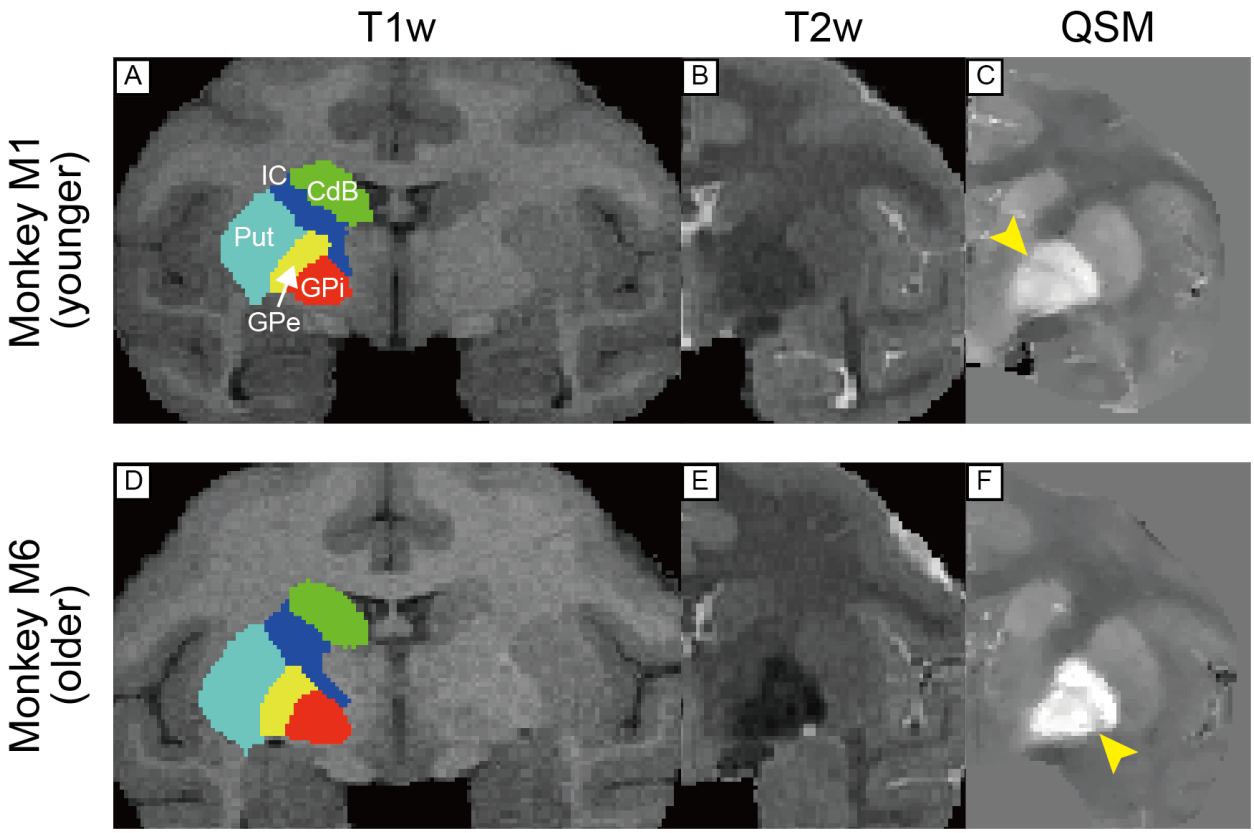

Figure 3. T1w, T2w, and QSM coronal images including borders of GPe and GPi in a younger ((A), (B), and (C)) and older monkeys ((D), (E), and (F)). Yellow arrow head in (C) and (F) indicates the medial medullary lamina. Abbreviations: CdB, body of caudate nucleus. GPe, globus pallidus external segment. GPi, globus pallidus internal segment. IC, internal capsule. Put, putamen.

bioRxiv preprint doi: https://doi.org/10.1101/2021.04.17.440277; this version posted April 19, 2021. The copyright holder for this preprint (which was not certified by peer review) is the author/funder. All rights reserved. No reuse allowed without permission.

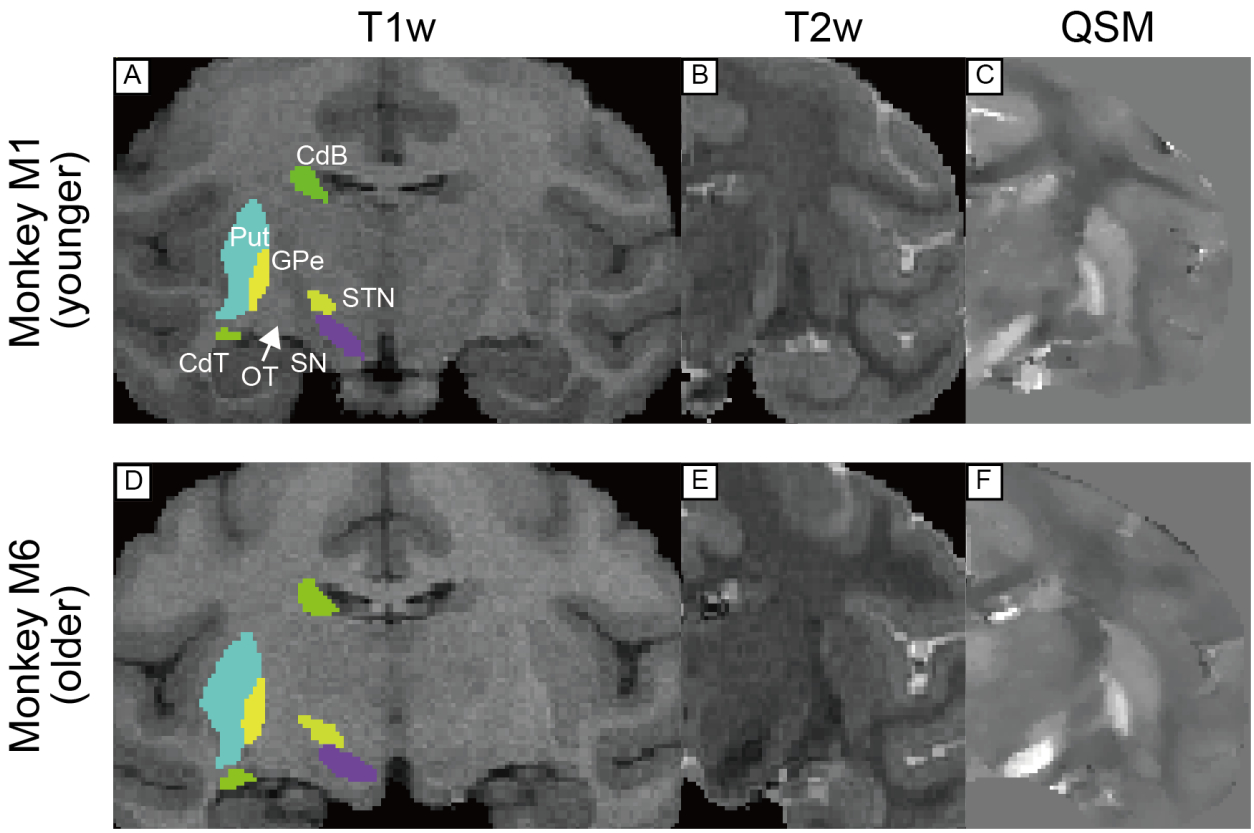

371

372 **Figure 4.** T1w, T2w, and QSM coronal images including substantia nigra in a younger ((A), (B),

373 and (C)) and older monkeys ((D), (E), and (F)). Abbreviations: CdB, body of caudate nucleus.

374 CdT, tail of caudate nucleus. GPe, globus pallidus external segment. OT, optic tract. Put,

375 putamen. SN, substantia nigra. STN, subthalamic nucleus.

376

bioRxiv preprint doi: https://doi.org/10.1101/2021.04.17.440277; this version posted April 19, 2021. The copyright holder for this preprint (which was not certified by peer review) is the author/funder. All rights reserved. No reuse allowed without permission.

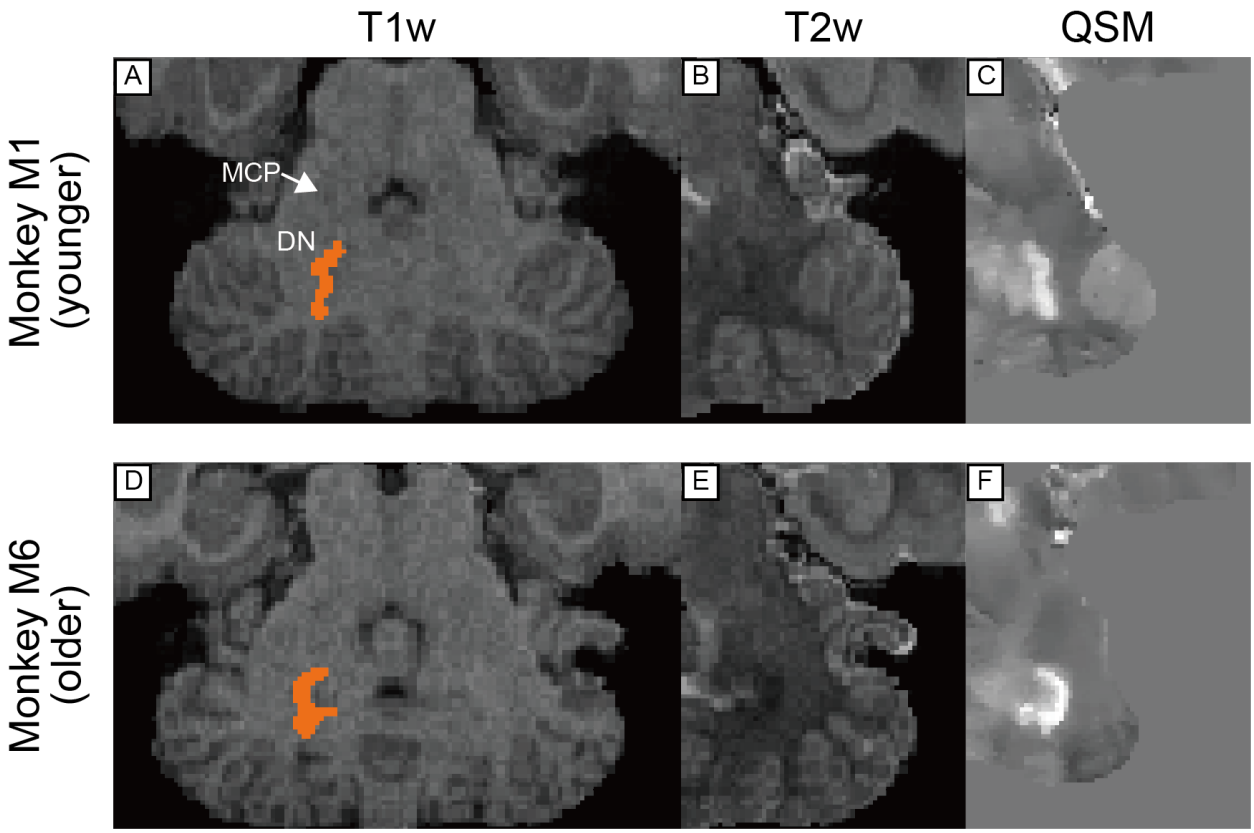

Figure 5. T1w, T2w, and QSM transverse images including dentate nucleus in cerebellum in a younger ((A), (B), and (C)) and older monkeys ((D), (E), and (F)). Abbreviations: DN, dentate nucleus. MCP, middle cerebellar peduncle.

bioRxiv preprint doi: https://doi.org/10.1101/2021.04.17.440277; this version posted April 19, 2021. The copyright holder for this preprint (which was not certified by peer review) is the author/funder. All rights reserved. No reuse allowed without permission.

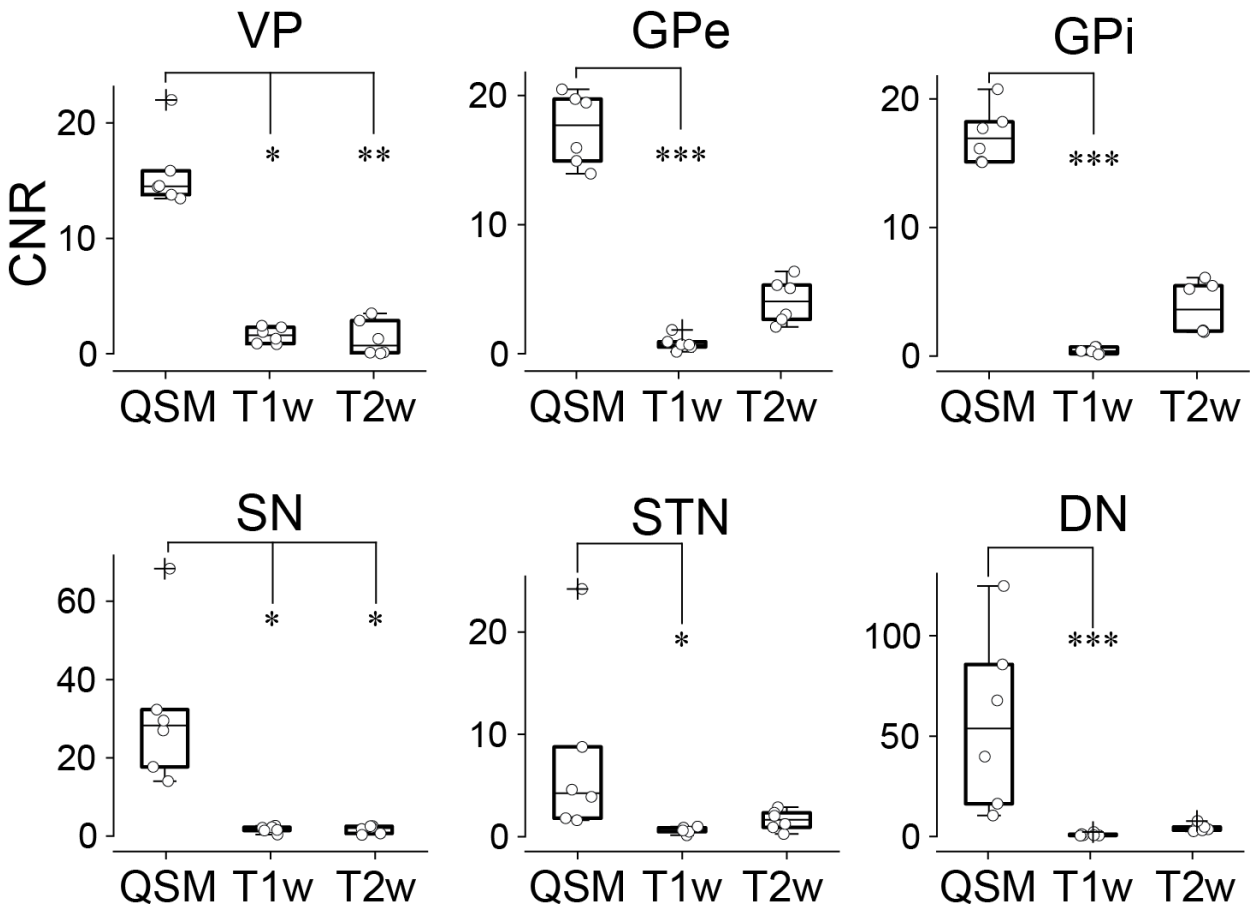

Figure 6. Comparison of CNR among subcortical regions in T1w, T2w, and QSM. In the box plots, upper and lower lines indicate the 75th and 25th percentile respectively, and dot line shows the median. Whiskers above and below the box represent the 10th and 90th percentiles. The cross sign indicates the outliers and the circle the CNR value of each data. Differences of CNR among images were assessed using Kruskal-Wallis test and post hoc test (Dunn-Sidak) (*$P < 0.05$, ** $P < 0.01$, ***$P < 0.001$). Abbreviations: DN, dentate nucleus. GPe, globus pallidus external segment. GPi, globus pallidus internal segment. SN, substantia nigra. STN, subthalamic nucleus. VP, ventral pallidum.

bioRxiv preprint doi: https://doi.org/10.1101/2021.04.17.440277; this version posted April 19, 2021. The copyright holder for this preprint (which was not certified by peer review) is the author/funder. All rights reserved. No reuse allowed without permission.

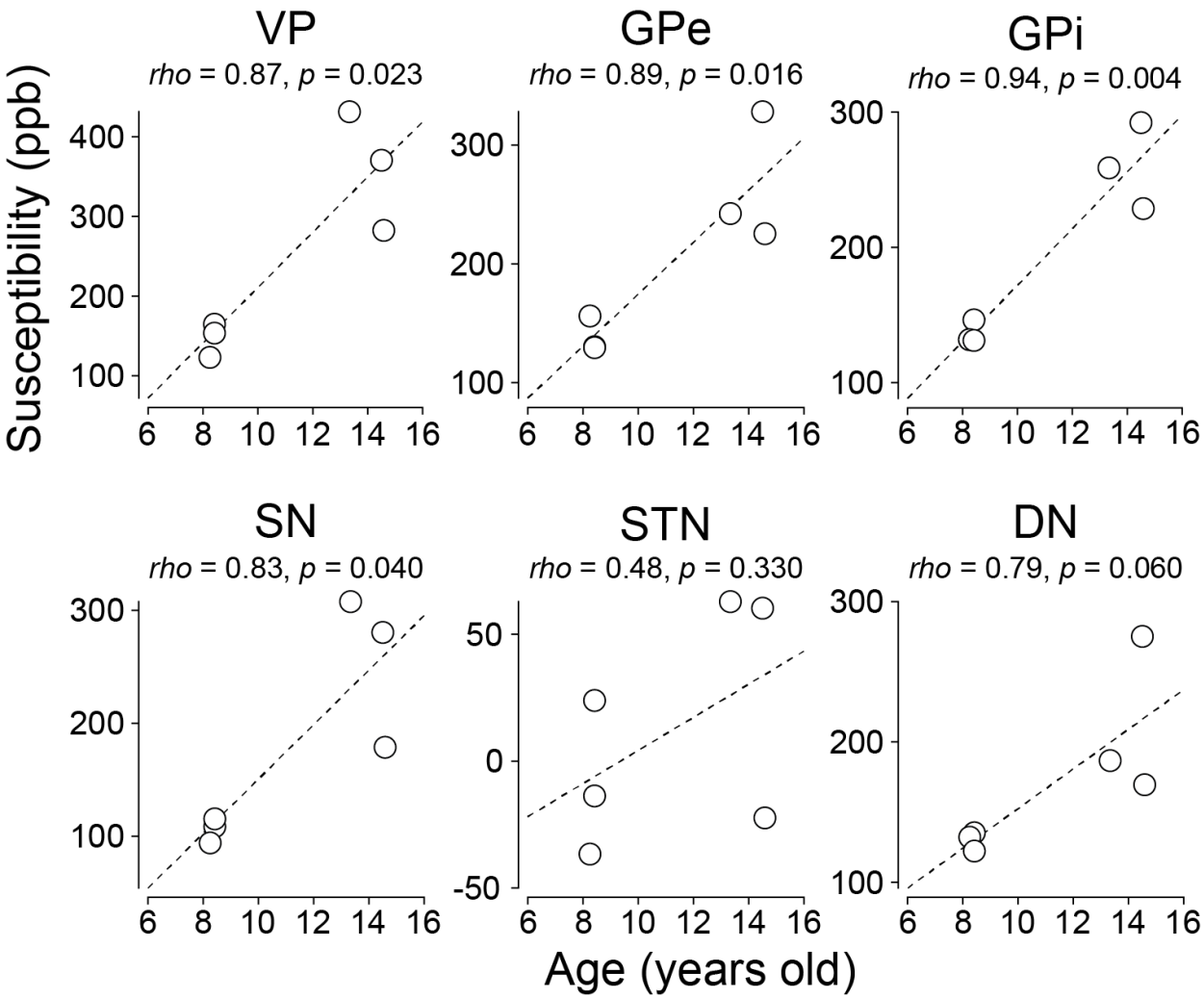

Figure 7. Correlation between monkeys' ages and mean QSM values of subcortical areas. Each circle indicates the mean QSM value of individual subcortical ROIs and the dash line represents regression slope.

bioRxiv preprint doi: https://doi.org/10.1101/2021.04.17.440277; this version posted April 19, 2021. The copyright holder for this preprint (which was not certified by peer review) is the author/funder. All rights reserved. No reuse allowed without permission.

403 ***Supplementary Figure***

404

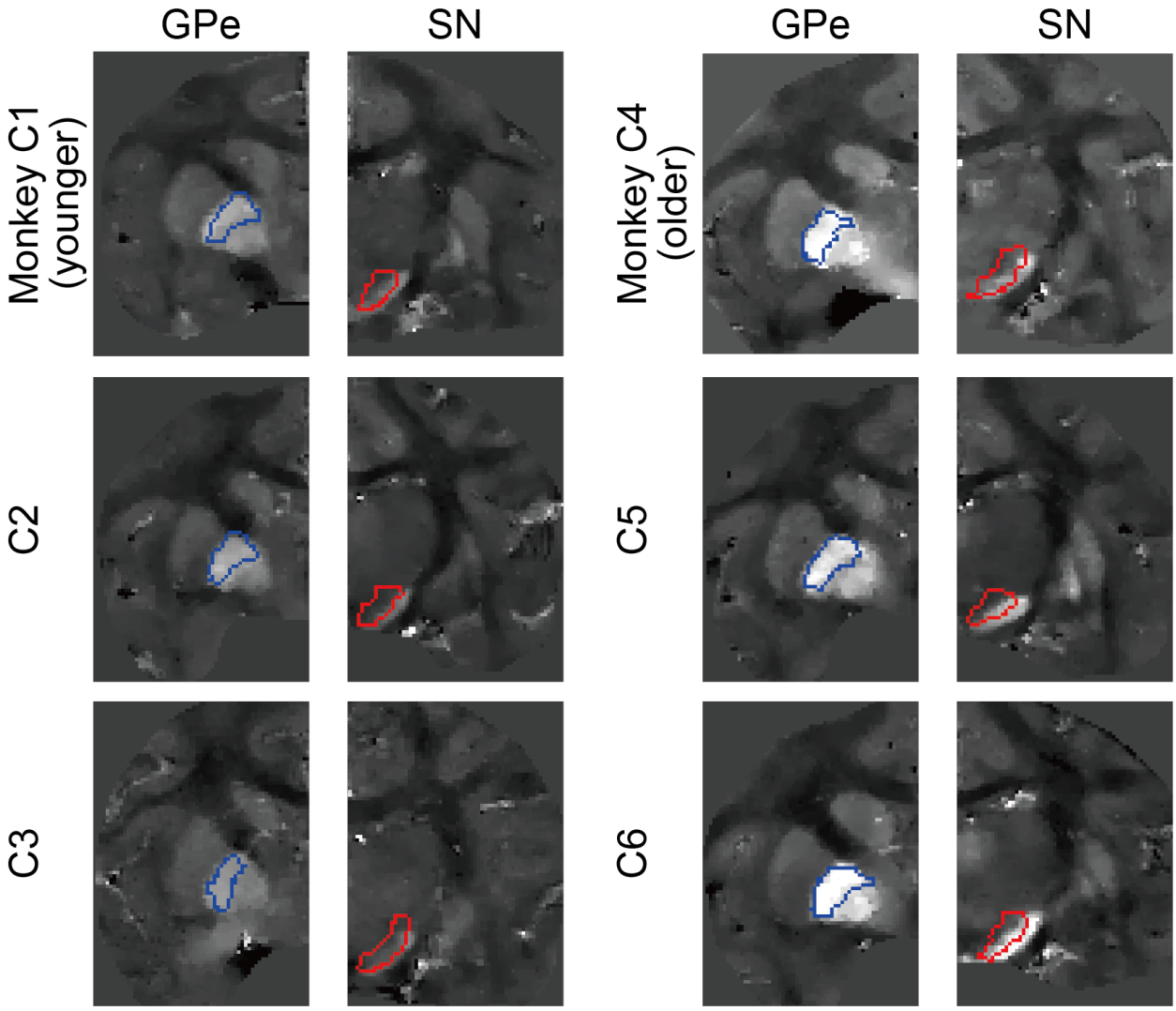

405

406 **Supplementary Figure 1.** Comparison of registered GPe and SN ROIs from the SARM atlas

407 with QSM images of all six monkeys (left hemisphere including the GPe and right hemisphere

408 with the SN). Blue- and red-colored enclosed areas imply the edges of the GPe and SN ROIs

409 created from the SARM atlas registration, respectively.

410

bioRxiv preprint doi: https://doi.org/10.1101/2021.04.17.440277; this version posted April 19, 2021. The copyright holder for this preprint (which was not certified by peer review) is the author/funder. All rights reserved. No reuse allowed without permission.

411 ***References***

412 Amita, H., Kim, H.F., Inoue, K.I., Takada, M., Hikosaka, O., 2020. Optogenetic manipulation of
413 a value-coding pathway from the primate caudate tail facilitates saccadic gaze shift. Nat.
414 Commun. 11, 1876.
415
416 Ashmore, R.C., Sommer, M.A., 2013. Delay activity of saccade-related neurons in the caudal
417 dentate nucleus of the macaque cerebellum. J. Neurophysiol. 109, 2129-2144.
418
419 Benjamini, Y., Hochberg, Y. 1995. Controlling the False Discovery Rate: a Practical and
420 Powerful Approach to Multiple Testing. J. R. Statist. Soc. B. 57, 289-300.
421
422 Bollmann, S., Rasmussen, K.G.B., Kristensen, M., Blendal, R.G., Østergaard, L.R., Plocharski,
423 M., O'Brien, K., Langkammer, C., Janke, A., Barth, M., 2019. DeepQSM - using deep learning
424 to solve the dipole inversion for quantitative susceptibility mapping. Neuroimage. 195, 373-383.
425
426 Bonaventura, J., Eldridge, M.A.G., Hu, F., Gomez, J.L., Sanchez-Soto, M., Abramyan, A.M.,
427 Lam, S., Boehm, M.A., Ruiz, C., Farrell, M.R., Moreno, A., Galal Faress, I.M., Andersen, N.,
428 Lin, J.Y., Moaddel, R., Morris, P.J., Shi, L., Sibley, D.R., Mahler, S.V., Nabavi, S., Pomper,
429 M.G., Bonci, A., Horti, A.G., Richmond, B.J., Michaelides, M., 2019. High-potency ligands for
430 DREADD imaging and activation in rodents and monkeys. Nat. Commun. 10, 4627.
431
432 Bostan, A.C., Strick, P.L., 2018. The basal ganglia and the cerebellum: nodes in an integrated
433 network. Nat. Rev. Neurosci. 19, 338-350.

bioRxiv preprint doi: https://doi.org/10.1101/2021.04.17.440277; this version posted April 19, 2021. The copyright holder for this preprint (which was not certified by peer review) is the author/funder. All rights reserved. No reuse allowed without permission.

Bilgic, B., Pfefferbaum, A., Rohlfing, T., Sullivan, E.V., Adalsteinsson, E., 2012. MRI estimates of brain iron concentration in normal aging using quantitative susceptibility mapping. Neuroimage 59, 2625-2635.

Cox, R.W., 1996. AFNI: software for analysis and visualization of functional magnetic resonance neuroimages. Compt. Biomed. Res. 29, 162-173.

Dimov, A.V., Gupta, A., Kopell, B.H., Wang, Y., 2018. High-resolution QSM for functional and structural depiction of subthalamic nuclei in DBS presurgical mapping. J. Neurosurg. 131, 360-367.

de Hollander, G., Keuken, M.C., Bazin, P.L., Weiss, M., Neumann, J., Reimann, K., Wähnert, M., Turner, R., Forstmann, B.U., Schäfer, A., 2014. A gradual increase of iron toward the medial-inferior tip of the subthalamic nucleus. Hum. Brain Mapp. 35, 4440-4449.

El-Shamayleh, Y., Horwitz, G.D., 2019. Primate optogenetics: Progress and prognosis. Proc. Natl. Acad. Sci. U. S. A. 116, 26195-26203.

Eldridge, M.A., Lerchner, W., Saunders, R.C., Kaneko, H., Krausz, K.W., Gonzalez, F.J., Ji, B., Higuchi, M., Minamimoto, T., Richmond, B.J., 2016. Chemogenetic disconnection of monkey orbitofrontal and rhinal cortex reversibly disrupts reward value. Nat. Neurosci. 19, 37-39.

bioRxiv preprint doi: https://doi.org/10.1101/2021.04.17.440277; this version posted April 19, 2021. The copyright holder for this preprint (which was not certified by peer review) is the author/funder. All rights reserved. No reuse allowed without permission.

457 Fredericks, J.M., Dash, K.E., Jaskot, E.M., Bennett, T.W., Lerchner, W., Dold, G., Ide, D.,
458 Cummins, A.C., Der Minassian, V.H., Turchi, J.N., Richmond, B.J., Eldridge, M.A.G., 2020.
459 Methods for mechanical delivery of viral vectors into rhesus monkey brain. J. Neurosci. Methods
460 339, 108730.
461
462 Hartig, R., Glen, D., Jung, B., Logothethis, N.K., Paxinos, G., Garza-Villarreal, E.A., Messinger,
463 A., Evrard, H.C., 2021. The Subcortical Atlas of the Rhesus Macaque (SARM) for
464 Neuroimaging. Neuroimage, 117996.
465
466 Ito, M., 2008. Control of mental activities by internal models in the cerebellum. Nat. Rev.
467 Neurosci. 9, 304-313.
468
469 Jung, B., Taylor, P., Seidlitz, J., Sponheim, C., Perkins, P., Ungerleider, L.G., Glen, D.,
470 Messinger, A., 2021. A comprehensive macaque fMRI pipeline and hierarchical atlas.
471 Neuroimage 117997.
472
473 Kueken, M.C., Bazin, P-L., Backhouse, K., Beekhuizen, S., Himmer, L., Kandola, A., Lafeber,
474 J.J., Prochazkova, L., Trutti, A., Schafer, A., Turner, R., Forstmann, B.U., 2017. Effects of aging
475 on T1, T2*, and QSM MRI values in the subcortex. Brain Struct. Funct. 222, 2487-2505.
476
477 Kunimatsu, J., Suzuki, T.W., Ohmae, S., Tanaka, M., 2018. Different contributions of
478 preparatory activity in the basal ganglia and cerebellum for self-timing. Elife 7, e35676.
479

bioRxiv preprint doi: https://doi.org/10.1101/2021.04.17.440277; this version posted April 19, 2021. The copyright holder for this preprint (which was not certified by peer review) is the author/funder. All rights reserved. No reuse allowed without permission.

480 Li, J., Li, Y., Gutierrez, L., Xu, W., Wu, Y., Liu, C., Li, D., Sun, B., Zhang, C., Wei, H., 2020.
481 Imaging the Centromedian Thalamic Nucleus Using Quantitative Susceptibility Mapping. Front.
482 Hum. Neurosci. 13, 447.
483
484 Li, W., Wu, B., Liu, C., 2011. Quantitative susceptibility mapping of human brain reflects spatial
485 variation in tissue composition. Neuroimage 55, 1645-1656.
486
487 Li, W., Wu, B., Batrachenko, A., Bancroft-Wu, V., Morey, R.A., Shashi, V., Langkammer, C.,
488 De Bellis, M.D., Ropele, S., Song, A.W., Liu, C. 2014. Differential developmental trajectories of
489 magnetic susceptibility in human brain gray and white matter over the lifespan. Hum. Brain
490 Mapp. 35, 2698-2713.
491
492 Liu, C., Li, W., Tong, K.A., Yeom, K.W., Kuzminski, S., 2015. Susceptibility-weighted imaging
493 and quantitative susceptibility mapping in the brain. J. Magn. Reson. Imaging 42, 23-41.
494
495 Liu, J., Liu, T., de Rochefort, L., Ledoux, J., Khalidov, I., Chen, W., Tsiouris, A.J., Wisnieff, C.,
496 Spincemaille, P., Prince, M.R., Wang, Y., 2012. Morphology enabled dipole inversion for
497 quantitative susceptibility mapping using structural consistency between the magnitude image
498 and the susceptibility map. Neuroimage 59, 2560-2568.
499
500 Liu, T., Spincemaille, P., de Rochefort, L., Kressler, B., Wang, Y., 2009. Calculation of
501 susceptibility through multiple orientation sampling (COSMOS): a method for conditioning the

bioRxiv preprint doi: https://doi.org/10.1101/2021.04.17.440277; this version posted April 19, 2021. The copyright holder for this preprint (which was not certified by peer review) is the author/funder. All rights reserved. No reuse allowed without permission.

inverse problem from measured magnetic field map to susceptibility source image in MRI. Magn. Reson. Med. 61, 196-204.

Liu, T., Liu, J., de Rochefort, L., Spincemaille, P., Khalidov, I., Ledoux, J.R., Wang, Y., 2011. Morphology enabled dipole inversion (MEDI) from a single-angle acquisition: comparison with COSMOS in human brain imaging. Magn. Reson. Med. 66, 777-783.

Liu, T., Wisnieff, C., Lou, M., Chen, W., Spincemaille, P., Wang, Y., 2013a. Nonlinear formulation of the magnetic field to source relationship for robust quantitative susceptibility mapping. Magn. Reson. Med. 69, 467-476.

Liu, T., Eskreis-Winkler, S., Schweitzer, A.D., Chen, W., Kaplitt, M.G., Tsiouris, A.J., Wang, Y., 2013b. Improved subthalamic nucleus depiction with quantitative susceptibility mapping. Radiology 269, 216-223.

Liu, Z., Spincemaille, P., Yao, Y., Zhang, Y., Wang, Y., 2018. MEDI+0: Morphology enabled dipole inversion with automatic uniform cerebrospinal fluid zero reference for quantitative susceptibility mapping. Magn. Reson. Med. 79, 2795-2803.

Lu, X., Hikosaka, O., Miyachi, S., 1998. Role of monkey cerebellar nuclei in skill for sequential movement. J. Neurophysiol. 79, 2245-2254.

bioRxiv preprint doi: https://doi.org/10.1101/2021.04.17.440277; this version posted April 19, 2021. The copyright holder for this preprint (which was not certified by peer review) is the author/funder. All rights reserved. No reuse allowed without permission.

524 Maeda, K., Inoue, K.I., Kunimatsu, J., Takada, M., Hikosaka, O., 2020. Primate Amygdalo-
525 Nigral Pathway for Boosting Oculomotor Action in Motivating Situations. iScience 23, 101194.
526
527 Middleton, F.A, Strick, P.L., 2001. Cerebellar Projections to the Prefrontal Cortex of the
528 Primate. J. Neurosci. 21, 700-712.
529
530 Mugler, J.P. 3rd, Bao, S., Mulkern, R.V., Guttmann, C.R., Robertson, R.L., Jolesz, F.A.,
531 Brookeman, J.R., 2000. Optimized single-slab three-dimensional spin-echo MR imaging of the
532 brain. Radiology 216, 891-899.
533
534 Nagai, Y., Kikuchi, E., Lerchner, W., Inoue, K.I., Ji, B., Eldridge, M.A., Kaneko, H., Kimura,
535 Y., Oh-Nishi, A., Hori, Y., Kato, Y., Hirabayashi, T., Fujimoto, A., Kumata, K., Zhang, M.R.,
536 Aoki, I., Suhara, T., Higuchi, M., Takada, M., Richmond, B.J., Minamimoto, T., 2016. PET
537 imaging-guided chemogenetic silencing reveals a critical role of primate rostromedial caudate in
538 reward evaluation. Nat. Commun. 7, 13605.
539
540 Ohmae, S., Uematsu, A., Tanaka, M., 2013. Temporally specific sensory signals for the detection
541 of stimulus omission in the primate deep cerebellar nuclei. J. Neurosci. 33, 15432-15441.
542
543 Persson, N., Wu, J., Zhang, Q., Liu, T., Shen, J., Bao, R., Ni, M., Liu, T., Wang, Y.,
544 Spincemaille, P., 2015. Age and sex related differences in subcortical brain iron concentrations
545 among healthy adults. Neuroimage 122, 385-398.
546

bioRxiv preprint doi: https://doi.org/10.1101/2021.04.17.440277; this version posted April 19, 2021. The copyright holder for this preprint (which was not certified by peer review) is the author/funder. All rights reserved. No reuse allowed without permission.

547 Schafer, A., Forstmann, B.U., Neumann, J., Wharton, S., Mietke, A., Bowtell, R., Turner, R.
548 2012. Direct visualization of the subthalamic nucleus and its iron distribution using high-
549 resolusion susceptibility mapping. Hum. Brain Mapp. 33, 2831-2842.
550
551 Schweser, F., Deistung, A., Lehr, B.W., Reichenbach, J.R., 2011. Quantitative imaging of
552 intrinsic magnetic tissue properties using MRI signal phase: an approach to in vivo brain iron
553 metabolism? Neuroimage 54, 2789-2807.
554
555 Seidlitz, J., Sponheim, C., Glen, D., Ye, F.Q., Saleem, K.S., Leopold, D.A., Ungerleider, L.,
556 Messinger, A., 2018. A population MRI brain template and analysis tools for the macaque.
557 Neuroimage 170, 121-131.
558
559 Strick, P.L., Dum, R.P., Fiez, J.A., 2009. Cerebellum and nonmotor function. Annu. Rev.
560 Neurosci. 32, 413-434.
561
562 Tang, J., Liu, S., Neelavalli, J., Cheng, Y.C., Buch, S., Haacke, E.M., 2013.
563 Improving susceptibility mapping using a threshold-based K-space/image domain iterative
564 reconstruction approach. Magn. Reson. Med. 69, 1396-1407.
565
566 Wang, Y., Liu, T., 2015. Quantitative susceptibility mapping (QSM): Decoding MRI data for a
567 tissue magnetic biomarker. Magn. Reson. Med. 73, 82-101.
568

bioRxiv preprint doi: https://doi.org/10.1101/2021.04.17.440277; this version posted April 19, 2021. The copyright holder for this preprint (which was not certified by peer review) is the author/funder. All rights reserved. No reuse allowed without permission.

569 Wei, H., Zhang, C., Wang, T., He, N., Li, D., Zhang, Y., Liu, C., Yan, F., Sun, B., 2019. Precise
570 targeting of the globus pallidus internus with quantitative susceptibility mapping for deep brain
571 stimulation surgery. J. Neurosurg. 191254.
572
573 Wen, Q., Yang, H., Zhong, K., 2019. Quantitative susceptibility mapping of ultra-high resolution
574 monkey brain in vivo at 9.4 T. Sheng Wu Yi Xue Gong Cheng Xue Za Zhi. 36, 349-355.
575
576 Wharton, S., Schäfer, A., Bowtell, R., 2010. Susceptibility mapping in the human brain using
577 threshold-based k-space division. Magn. Reson. Med. 63, 1292-1304.
578
579 Wu, B., Li, W., Guidon, A., Liu, C., 2012. Whole brain susceptibility mapping using compressed
580 sensing.
581 Magn. Reson. Med. 67, 137-147.
582